Evaporation of Water from Airborne Droplets Containing Sodium Chloride, Mucin, and Surfactant

Keita Kurai, Hikaru Miyamoto, Nobuyuki Takegawa [ORCID]*

Department of Chemistry, Graduate School of Science, Tokyo Metropolitan University, Hachioji, Tokyo 192-0397, Japan

ABSTRACT

We conducted laboratory experiments to investigate the evaporation of water from airborne model respiratory droplets containing sodium chloride (NaCl) as an inorganic salt, mucin as a glycoprotein, and dipalmitoylphosphatidylcholine (DPPC) as a surfactant. The model respiratory droplets were introduced into a flow tube, in which the relative humidity (RH) was controlled at 30%, 50%, and 70%. The residence time of the model droplets under the RH-controlled conditions was altered by varying the length of the flow tube. Size-segregated particle number concentrations were measured using an optical particle counter placed at the end of the flow tube vented to the atmosphere. The particle number size distributions for NaCl exhibited systematic changes with an increasing RH. The particle number size distributions for (NaCl + mucin) and (NaCl + mucin + DPPC) exhibited very weak RH dependency. These results suggest that the presence of mucin and DPPC had a significant effect on the RH dependency of the evaporation of water from the model droplets.

Keywords: Respiratory droplets, Relative humidity, Glycoprotein, Surfactant

1 INTRODUCTION

The coronavirus disease 2019 (COVID-19) caused by the severe acute respiratory syndrome coronavirus 2 (SARS-CoV-2) has seriously affected society since its global outbreak in early 2020 (WHO, 2020). Many attempts have been made to investigate the modes of transmission of SARS-CoV-2 (e.g., Leung, 2021; Meister et al., 2022; Piana et al., 2021; Zhou et al., 2021). The dynamics of respiratory droplets in air have drawn considerable attention since airborne transmission was recognized as an important route (e.g., Morawska and Milton, 2020; Rezaei and Netz, 2021), and evidence has emerged that airborne transmission is the major route of the spread of COVID-19 (Wang et al., 2021, and references therein).

The lifetime of respiratory droplets in ambient air is controlled by the initial size of the droplets upon emission, the airflow dynamics, and the evaporation of water from the droplets. A large fraction of respiratory droplets can originate from saliva, which contains various substances, including inorganic ions, glycoproteins, surfactants, and enzymes (Yang and Marr, 2012; Vejerano and Marr, 2018). The evaporation rate of water from respiratory droplets depends on the size and chemical composition of the droplets and the ambient relative humidity (RH). The evaporation of water from droplets containing inorganic salts for a given RH condition can be theoretically predicted, whereas that from droplets containing organic compounds is not fully understood. In a mixed solution of inorganic salts and organic matter, liquid-liquid phase separation might result in the formation of an organic-rich shell on an inorganic-rich core (Liu et al., 2018; Freedman, 2020; Mikhailov et al., 2021). Ambient RH is also important in considering the fate of viral infectivity, although the mechanisms that affect the RH dependency of viral infectivity are poorly understood (e.g., Yang and Marr, 2011; Kormuth et al., 2018; Prussin et al., 2018; Robey and Fierce, 2022; Lin et al., 2020; Božič and Kanduč, 2021; Morris et al., 2021).

The physicochemical properties of respiratory droplets have been investigated in the laboratory.

Several studies have used model respiratory droplets (~10–100 µm) containing sodium chloride (NaCl) as an inorganic salt, mucin or albumin as a protein, and dipalmitoylphosphatidylcholine (DPPC) or sodium dodecyl sulfate as a surfactant (Vejerano and Marr 2018; Lin *et al.*, 2020; Davies *et al.*, 2021; Seyfert *et al.*, 2022). Vejerano and Marr (2018) used solutions containing NaCl, (NaCl + mucin), and (NaCl + mucin + DPPC) as model droplets. They investigated changes in the size and structure of the model droplets deposited on super hydrophobic substrates under RH-controlled conditions and found that loss of water induced phase separation of the components.

Levitation techniques have been used for investigating the evaporation processes of water from airborne droplets (e.g., Lieber *et al.*, 2021; Davies *et al.*, 2021; Huynh *et al.*, 2022). Lieber *et al.* (2021) used human saliva droplets and showed that the time required for the loss of the majority of water from saliva droplets agreed well with that from pure water droplets and was approximately proportional to the square of the initial diameter (known as the classical D^2-law). Davies *et al.* (2021) used simulated lung fluid droplets, the major components of which included NaCl, sodium bicarbonate ($NaHCO_3$), mucin, and DPPC, and showed that RH history is important in controlling the state of respiratory droplets. Huynh *et al.* (2022) investigated the structural changes in evaporating droplets containing NaCl and protein and found that a protein-enriched shell with aqueous inorganic core could be formed in a droplet during the evaporation of water.

The above-mentioned laboratory studies have provided useful insights into the dynamics of respiratory droplets in the atmosphere. The key findings obtained from those studies include that (1) airborne droplets (pure water, NaCl solution, saliva proxy, and real human saliva) tend to lose a significant amount of water within short time (< 1 s for 10-µm droplets) at ambient RH levels (~50%); (2) the amount of residual water under equilibrium RH conditions depends on the chemical compositions; and (3) the phase of saliva or saliva proxy droplets can change from liquid to semi-solid (amorphous) or solid states, depending on the chemical compositions and equilibrium RH. However, the effects of glycoproteins and surfactants on the evaporation of water from airborne droplets under various RH conditions are highly complex and are not well understood.

The purpose of the present study was to investigate the variability in the particle number size distributions of model respiratory droplets containing NaCl, mucin, and DPPC by varying the residence time and RH. We tested airborne NaCl, (NaCl + mucin), and (NaCl + mucin + DPPC) droplets to investigate the effects of glycoproteins and surfactants on the water evaporation in relation with the residence time and RH. To our knowledge, such experimental approach has not been previously reported. We focus on the particle diameter of the order of microns and the residence time of the order of seconds, which could be important in short-distance airborne transmission under real-world conditions.

2 METHODS

2.1 Preparation of Solutions

The chemical composition of the test solutions used in the present study was similar to that reported by Vejerano and Marr (2018). We used mucin derived from porcine stomach (Fujifilm Wako Pure Chemical Corporation, Japan) and DPPC (Echelon Biosciences, Inc., USA). Table 1 lists the combinations of chemicals, which include Solution A (NaCl 1 g L^{-1}), Solution B (NaCl 1 g L^{-1} + mucin 3 g L^{-1}), and Solution C (NaCl 1 g L^{-1} + mucin 3 g L^{-1} + DPPC 0.5 g L^{-1}). We also tested Solution C' (NaCl 1 g L^{-1} + mucin 3 g L^{-1} + DPPC 1 g L^{-1}) to further investigate the role of DPPC. However, we visually observed bubbles on the liquid surface during the nebulization of Solution C', which was probably due to stronger surfactant effects of DPPC for Solution C' than those for Solution C. The particle number concentrations for Solution C' were not stable, and thus we did

Table 1. Chemical compositions of each solution.

	Solution A	Solution B	Solution C
NaCl (g L^{-1})	1	1	1
Mucin (g L^{-1})	None	3	3
DPPC (g L^{-1})	None	None	0.5
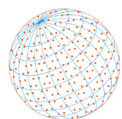
not use the Solution C' data in the present study. The NaCl concentration of 1 g L^{-1} was lower than that presented by Vejerano and Marr (2018) (9 g L^{-1}) and closer to the NaCl and KCl concentrations of artificial saliva presented by Walker *et al.* (2021) (0.88 and 1.04 g L^{-1}, respectively). Solutions B and C were stirred at room temperature for ~7 h using a magnetic stirrer to form a colloidal solution containing gel-like substances and were stored in a refrigerator to avoid degradation. Solutions B and C were further stirred just before the experiments, and a small volume of each solution was taken for the generation of droplets. The concentrations seemed to be rather inhomogeneous because of the presence of the gel-like substances originating from the mucin. Therefore, the absolute concentrations of mucin in the generated droplets may not have been precisely defined.

2.2 Flow Tube System

Fig. 1 shows the experimental apparatus for measuring the particle number concentrations with varying RH and residence time. The setup consists of a horizontally oriented stainless steel flow tube (inner diameter (ID): 55 mm), a conditioning flow for RH control, a glass nebulizer, a hygrometer (HMT337, Vaisala, Finland), and an optical particle counter (OPC) (HHPC6+, Beckman Coulter, Inc., USA). The flow tube is a combination of NW50 nipples, which enables adjustment of the length of the flow tube (*L*) from 10 to 100 cm. Polydisperse aerosol particles were generated from the test solution using a glass nebulizer at a flow rate of 1.6–3.0 L min^{-1}. The conditioning flow rate was adjusted to ~11.8 L min^{-1} by mixing particle-free dry air with particle-free humidified air. Humidification was achieved by bubbling a water flask using particle-free air. The RH in the flow tube was controlled by varying the mixing ratio of the dry and humidified air. The flow rates of the dry and humidified air were regulated using mass flow controllers (MFCs) upstream from the flask. The conditioning flow was injected from the outer side of the flow tube. The injection port of the aerosol flow was set at a slightly off-center position.

The exit port of the flow tube was vented to the atmosphere and enclosed by a hood. The inlet of the OPC was inserted from the exit port of the flow tube to measure the particle number concentrations at the radial center position. The hygrometer was placed at ~17 mm from the center of the flow tube to measure the RH. The OPC can quantify the particle number concentrations with six channels classified by the particle diameter (D_p) (ch1: $D_p \geq 0.3$ μm; ch2: $D_p \geq 0.5$ μm; ch3: $D_p \geq 1.0$ μm; ch4: $D_p \geq 2.0$ μm; ch5: $D_p \geq 5.0$ μm; and ch6: $D_p \geq 10$ μm). The data were recorded every 10 s with a sample flow rate of ~2.8 L min^{-1}.

The total particle number concentrations measured by the OPC (ch1; $D_p \geq 0.3$ μm) should not exceed 1.5×10^5 L^{-1} to avoid particle coincidence in the optical sensing volume. We used an additional flow controller (rotameter + valve) to regulate excess flow (1.4 L min^{-1}) for reducing the number of particles introduced into the flow tube. We set the total flow rate through the flow tube (sum of the aerosol and conditioning flow rates) to 12–14 L min^{-1}, and thus the residence time of air in the flow tube was primarily controlled by the length of the flow tube.
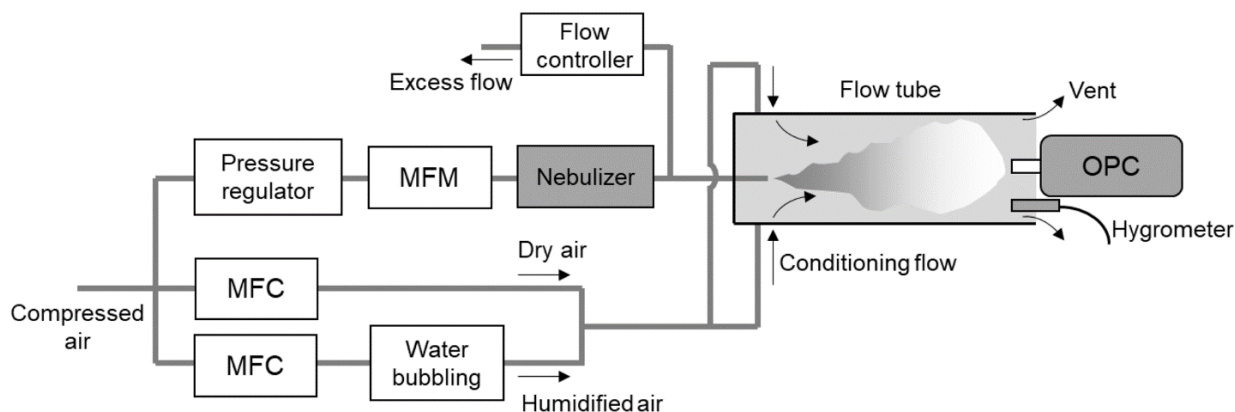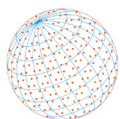

Fig. 1. Schematic diagram of the experimental apparatus. MFC: mass flow controller; MFM: mass flow meter; OPC: optical particle counter.

A flow rate of 12 L min⁻¹ and tube inner diameter of 55 mm yield an average Reynolds number in the flow tube of ~3×10^2, indicating a laminar flow regime. Therefore, the air velocity along the centerline axis was twice the average air velocity estimated from the flow rate and the cross-section area of the flow tube. The residence time of air along the centerline axis, t, was estimated to be 0.5–0.6 s for a flow tube length of 10 cm. We set the L values at 20, 40, and 60 cm, corresponding to the t values of 1, 2, and 3 s. We set the RH values at 30%, 50%, and 70% at a given t value (i.e., for a given flow tube length). The temperature of the flow tube ranged from 16°C to 22°C during the experiment. The size distributions of the original droplets generated by the nebulizer were not measured, which limited the interpretation of early-stage evaporation of water.

2.3 Data Analysis
2.3.1 RH dependency

The RH-dependent datasets were obtained for a given length of the flow tube and a solution type. The RH modulation cycle of each dataset consisted of 5 min data for each RH set point at 70%, 50%, 30%, and 70% (RH 70% data were duplicated for checking reproducibility), resulting in a total measurement time of ≤ 30 min per dataset. We selected a 3 min time period from the 5 min data for the size distribution analysis presented in Section 3.2. The particle number concentrations from neighboring channels of the OPC were differentiated to obtain "approximate" $dN/d\log D_p$ values. The size resolution of the OPC is relatively coarse, and no inversion analysis was performed for retrieval of the approximate $dN/d\log D_p$ values. We did not use the size bin derived from ch5 and ch6 (5–10 μm) because of the low particle number concentrations and potential sampling biases for larger particles in the horizontal direction (gravitational settling velocity for 10-μm particles is ~3 mm s⁻¹).

Preliminary experiments showed that the RH was nearly homogeneous in the cross section of the flow tube. On the other hand, the particle number concentrations were not homogeneous in the cross section of the flow tube. The difference in the homogeneity was likely due to the difference in the diffusion time scale between the water vapor and the particles. Therefore, the approximate $dN/d\log D_p$ values obtained at different RH values may not be simply comparable.

Let $n(D_p, \text{RH}, s)$ be the "true" $dN/d\log D_p$ values that are expected at a given RH value and a sampling point s in the cross section of the flow tube. Assuming that the particle loss in the flow tube was negligible, the integral of $n(D_p, \text{RH}, s)$ over the full size range averaged over the cross section of the flow tube (area S), N_0, is constant:

$$N_0 = \frac{1}{S} \int ds \int n\left(D_p, \text{RH}, s\right) d\log D_p. \tag{1}$$

The spatial homogeneity of the particle number concentrations over the cross section may depend on D_p for smaller (< 0.01 μm) and larger (> 10 μm) particles due to Brownian diffusion and gravitational settling, respectively. Here, we consider the range of D_p where the homogeneity does not significantly depend on D_p (0.3–5 μm). Let $r(\text{RH}, s)$ be the fraction of particles sampled at a given RH and a point s, which is an indicator of homogeneity. Even for a fixed sampling point, the $r(\text{RH}, s)$ values may vary depending on the RH. Here, we define the normalized particle number concentration, $\tilde{n}(D_p, \text{RH})$, as:

$$\tilde{n}\left(D_p, \text{RH}\right) = \frac{n\left(D_p, \text{RH}, s\right)}{N_0 r\left(\text{RH}, s\right)}. \tag{2}$$

The $\tilde{n}(D_p, \text{RH})$ values obtained at different RH values can be directly compared because the inhomogeneity of the particle number concentrations is taken into account. Let $f(D_p, \text{RH})$ be the ratio of $\tilde{n}(D_p, \text{RH})$ to $\tilde{n}(D_p, 30)$ values, where RH is either 50% or 70%:
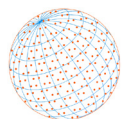
$$f\left(D_p, \text{RH}\right) = \frac{n\left(D_p, \text{RH}, s_0\right)}{n\left(D_p, 30, s_0\right)} \frac{r\left(30, s_0\right)}{r\left(\text{RH}, s_0\right)},\tag{3}$$

where s_0 is the center position at which the OPC inlet was placed. The $n(D_p, \text{RH}, s_0)/n(D_p, 30, s_0)$ ratio on the right-hand side of Eq. (3) can be estimated using the approximate $dN/d\log D_p$ values at selected D_p and RH values.

2.3.2 Hygroscopic growth

The OPC can detect particles with diameters larger than 0.3 µm. A shift in the particle size distributions to smaller sizes without any changes in the total particle number concentrations may lead to an apparent decrease in the particle number concentrations detected by the OPC. We measured the particle number size distributions with diameters ranging from 0.015 to 0.66 µm using a Scanning Mobility Particle Sizer (SMPS; Model 3936, TSI) consisting of a differential mobility analyzer (DMA; Model 3081, TSI) and a Condensation Particle Counter (CPC; Model 3022, TSI). The RH in the sheath flow of the SMPS was not controlled. Only data obtained at RH = 30% for Solution A were used for the analysis considering that a RH of 30% was below the efflorescence RH of NaCl particles (37–50%; Mikhailov *et al.*, 2004, and references therein). The inlet of the SMPS was placed ~17 mm from the center of the flow tube (similar to the hygrometer).

The SMPS data obtained at RH = 30% for Solution A were fitted by a lognormal function to estimate the geometric mean diameter (D_m) and geometric standard deviation (σ):

$$\frac{dN}{d\log D_p} = \frac{N_t}{\sqrt{2\pi}\log\sigma}\exp\left(-\frac{\left(\log D_p - \log D_m\right)^2}{2\log^2\sigma}\right),\tag{4}$$

where N_t is the total particle number concentration. The curve fitting algorithm with incorporation of the standard deviations of the experimental data (Igor Pro 8, WaveMetrics, Inc.) was used for the lognormal fitting. The D_m values derived from the lognormal fitting of the SMPS data (smaller than the detectable size range of the OPC) were used as a constraining factor for the lognormal fitting of the OPC data.

The particle size distributions at RH = 50% and 70% under equilibrium conditions were estimated from that at RH = 30% assuming a hygroscopic growth factor, which is defined as the ratio of wet (humidified) to dry diameters. Following Mikhailov *et al.* (2004), the hygroscopic growth factor for NaCl particles was assumed to be 1.5 and 1.7 at RH = 50% and 70%, respectively, during the efflorescence of NaCl particles with a dry diameter of ~0.1 µm.

3 RESULTS

3.1 Time Series

Figs. 2–4 show example time series of the particle number concentrations for Solution A (NaCl only), B (NaCl + mucin), and C (NaCl + mucin + DPPC) measured by the OPC at L = 60 cm (t = 3 s). The data obtained at L = 20 cm (t = 1 s) and 40 cm (t = 2 s) were similar to that at 60 cm (not shown). Only data with stable RH conditions (i.e., the RH values in the flow tube were reasonably well controlled near the set points) were used. The systematic bias (absolute value) of RH was smaller than ~1%, ~2%, and ~3% for a set point of RH = 30%, 50%, and 70%, respectively. The random error (relative value) of RH was smaller than ~1% of the set point. The variability in the RH values due to differences in the radial position of the flow tube, which can be caused by incomplete mixing of the nebulizer and conditioning flows, was found to be comparable to or smaller than the random error. The blank levels were measured without supplying particles from the nebulizer. They were less than 1% of the number concentrations of particles generated from the nebulizer for ch1–4 and nearly zero for ch5 and ch6, which had a minor effect on the interpretation of the particle measurement data. The data for RH = 70% obtained at the end of
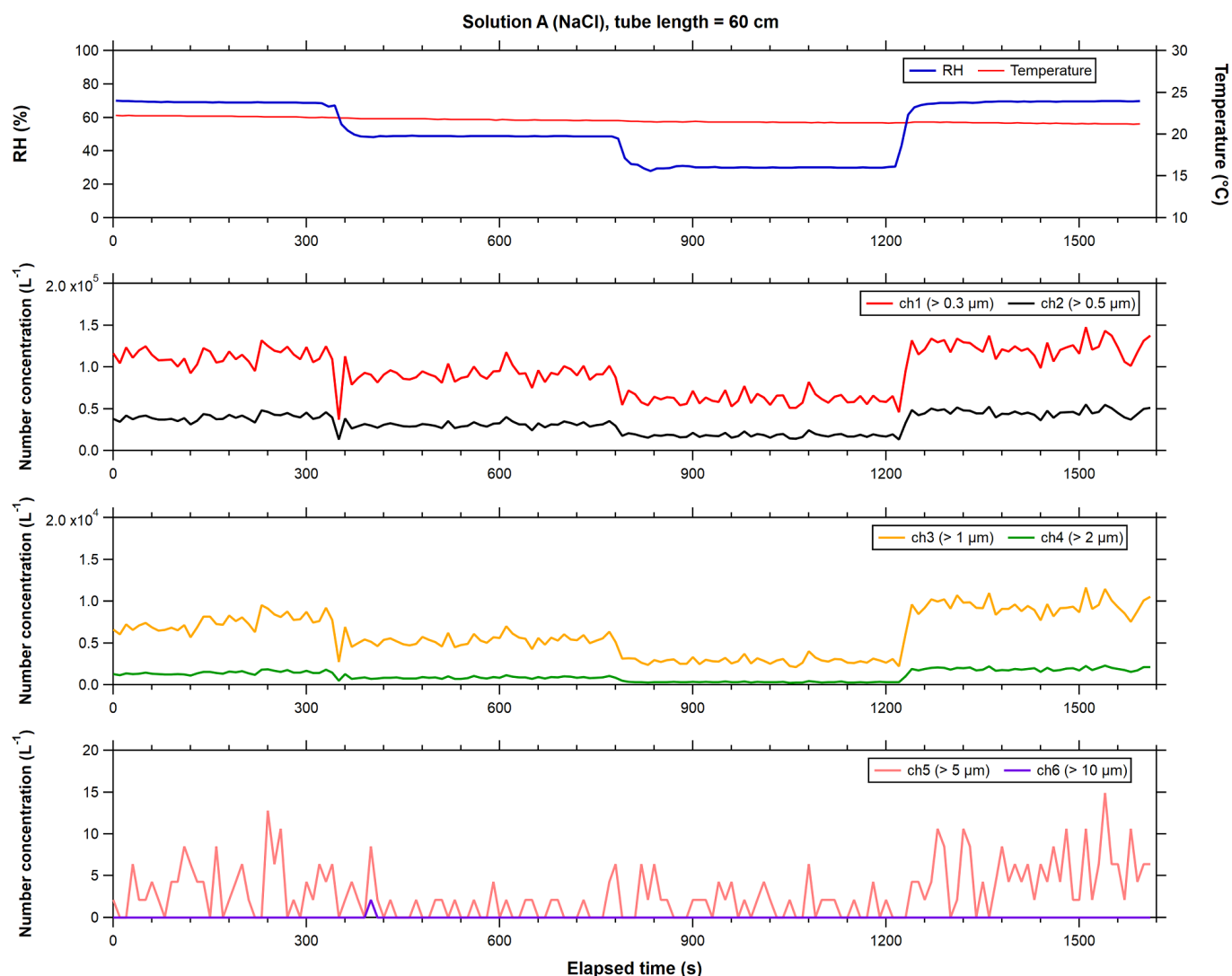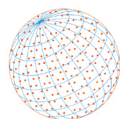
Fig. 2. Example time series of RH, temperature, and particle number concentrations for Solution A (NaCl) at a tube length (*L*) of 60 cm.

each cycle showed good agreement with that at the beginning for all the solutions, indicating the reproducibility of the measurements during each cycle.

The Solution A data (Fig. 2) showed systematic decreases in the particle number concentrations with a decreasing RH. The Solution B and C data showed decreasing trends in the particle number concentrations with a decreasing RH, but the RH dependency was weaker than that for Solution A (Fig. 3 and Fig. 4). The data for Solutions A and C showed spiked changes in the particle number concentrations for ch1–4 at an elapsed time of ~350 and ~1250 s, respectively, when RH was modulated. Spiked changes in the particle number concentrations were also observed upon changes in RH in other cases including Solution B. We consider that these features were due to the transient movement of spatially inhomogeneous particle number concentrations during the changes in RH.

3.2 Particle Number Size Distributions

Fig. 5 shows the particle number size distributions (approximate $dN/d\log D_p$ values) for Solutions A, B, and C measured by the OPC at *L* = 60 cm (*t* = 3 s). The data used in Fig. 5 are subsets of those used in Figs. 2–4; therefore, the RH dependency for the aerosol particles for Solutions A, B, and C inferred from Fig. 5 is basically the same as that from Figs. 2–4. As described in
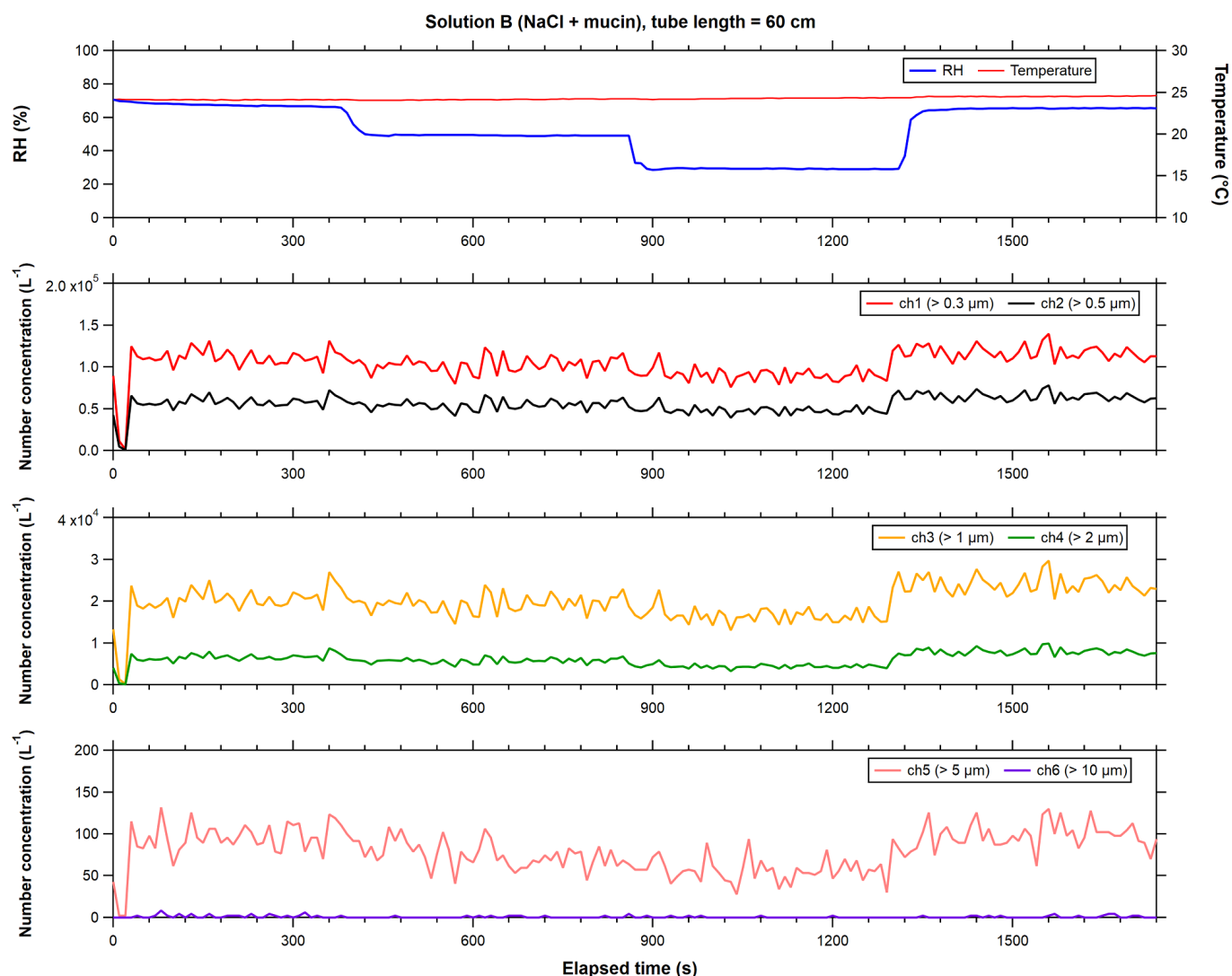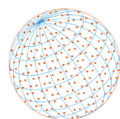
Fig. 3. Example time series of RH, temperature, and particle number concentrations for Solution B (NaCl + mucin) at *L* = 60 cm.

Section 2.3.1, the approximate dN/dlogD_p values obtained at different RH values cannot be simply compared because of the inhomogeneity of the particle number concentrations in the cross section of the flow tube as a function of RH.

Fig. 6(a) shows the particle number size distributions for Solution A measured by the SMPS and OPC at RH = 30% and *L* = 60 cm. The concentration of Solution A and the density of NaCl indicate that the diameter ratio of an original droplet to the completely dried particle is ~13. The original droplet diameters of 10 and 50 μm correspond to the dry diameters of ~0.77 and ~3.8 μm, respectively. These dry diameters are close to the upper end of the size range of the SMPS and OPC used in the current analysis, respectively. Using the simple mass transfer equations (Hinds, 1999), the time required for complete evaporation of pure water droplets, which is comparable to the time for water equilibrium for NaCl-containing droplets, is estimated to be ~0.1 and ~3 s for a droplet diameter of 10 and 50 μm, respectively, at RH = 30%. We can safely assume that the residence time of 3 s in the flow tube was sufficient for achieving water equilibrium for NaCl particles measured by the SMPS at RH = 30%. Because the RH of 30% was below the efflorescence RH of NaCl, the particles measured in the size range of the SMPS in Fig. 6(a) can be regarded as dry NaCl particles. There was a systematic difference in the absolute values between the SMPS and OPC data. Considering the difference in the sampling point between the SMPS and OPC, the difference may be due to the inhomogeneity of the particle number concentrations or the
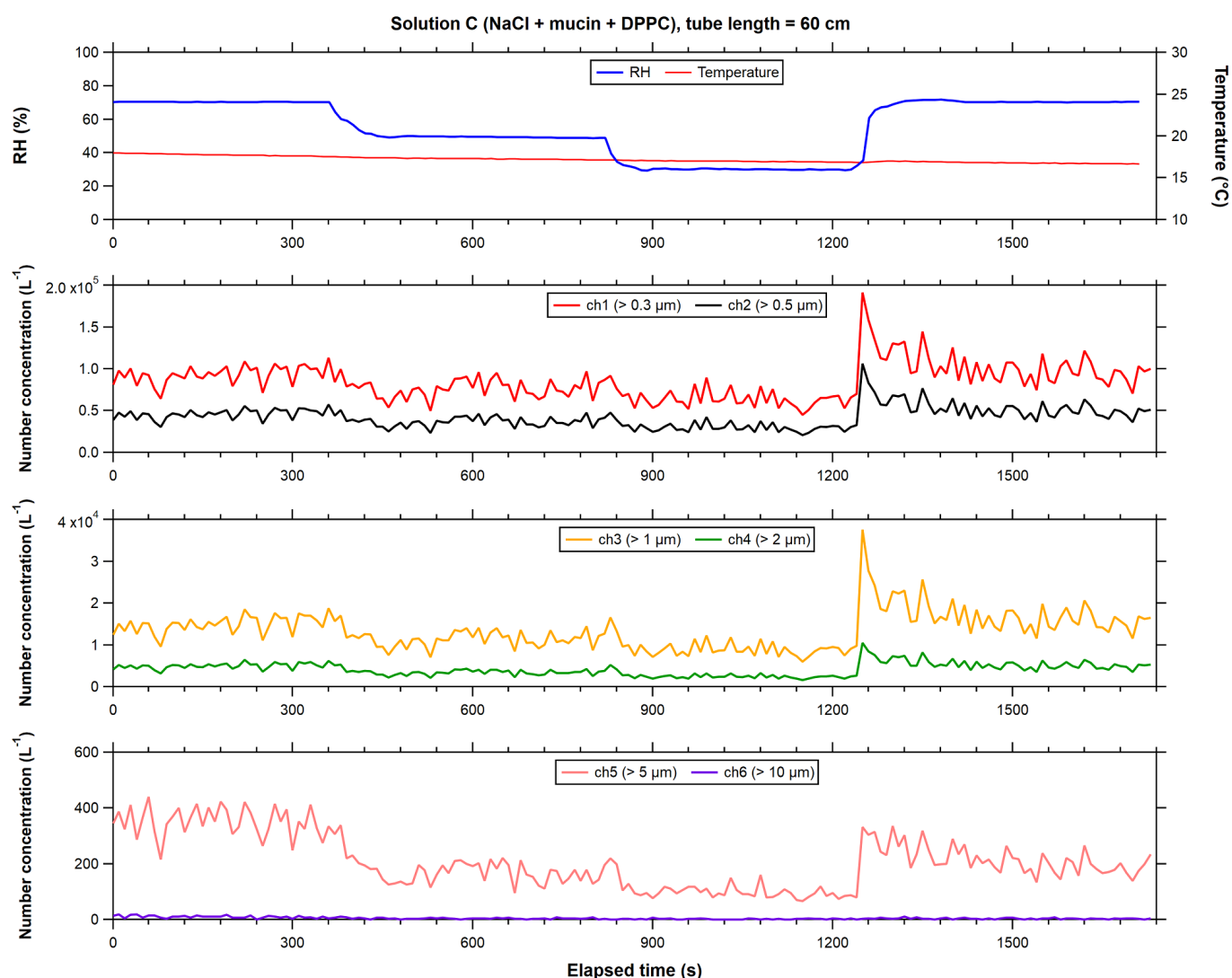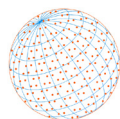
Fig. 4. Example time series of RH, temperature, and particle number concentrations for Solution C (NaCl + mucin + DPPC) at *L* = 60 cm.

difference between the mobility and the optical diameters (Chien *et al.*, 2016). The lognormal fitting for the SMPS data yielded $D_m = 0.055 \pm 0.004$ µm and $\sigma = 2.7 \pm 0.1$.

Fig. 6(b) shows the particle number size distributions (approximate $dN/d\log D_p$ values) for Solution A measured by the OPC at *L* = 60 cm. Based on the simple theoretical calculation described above, the particles measured in the size range of the OPC at RH = 30% in Fig. 6(b) can also be regarded as dry NaCl particles, except for those near the upper end of the size range. We investigate whether the RH dependency of the particle number size distributions could be explained by the hygroscopic properties of NaCl particles. The hygroscopic growth factors for NaCl particles are nearly constant for the diameter range discussed here (Zieger *et al.*, 2017). Therefore, the σ values for RH = 50% and 70% should be the same as that for RH = 30% under equilibrium conditions. We used the D_m value of 0.055 µm obtained from the SMPS and the hygroscopic growth factors described in Section 2.3.2 for constraining the lognormal fitting of the OPC data. Namely, we assumed $D_m = 0.055$, 0.083, and 0.094 µm for the lognormal fitting of the OPC data for RH = 30%, 50%, and 70%, respectively. The σ values determined from the fitting were 2.77 ± 0.05, 2.89 ± 0.04, and 3.13 ± 0.05 for RH = 30%, 50%, and 70%, respectively. The σ value for RH = 30% derived from the OPC was consistent with that derived from the SMPS. The σ values for RH = 50% and 70% were slightly larger (by a factor of ~1.04 and ~1.13, respectively) than that for RH = 30%. This point will be discussed later.
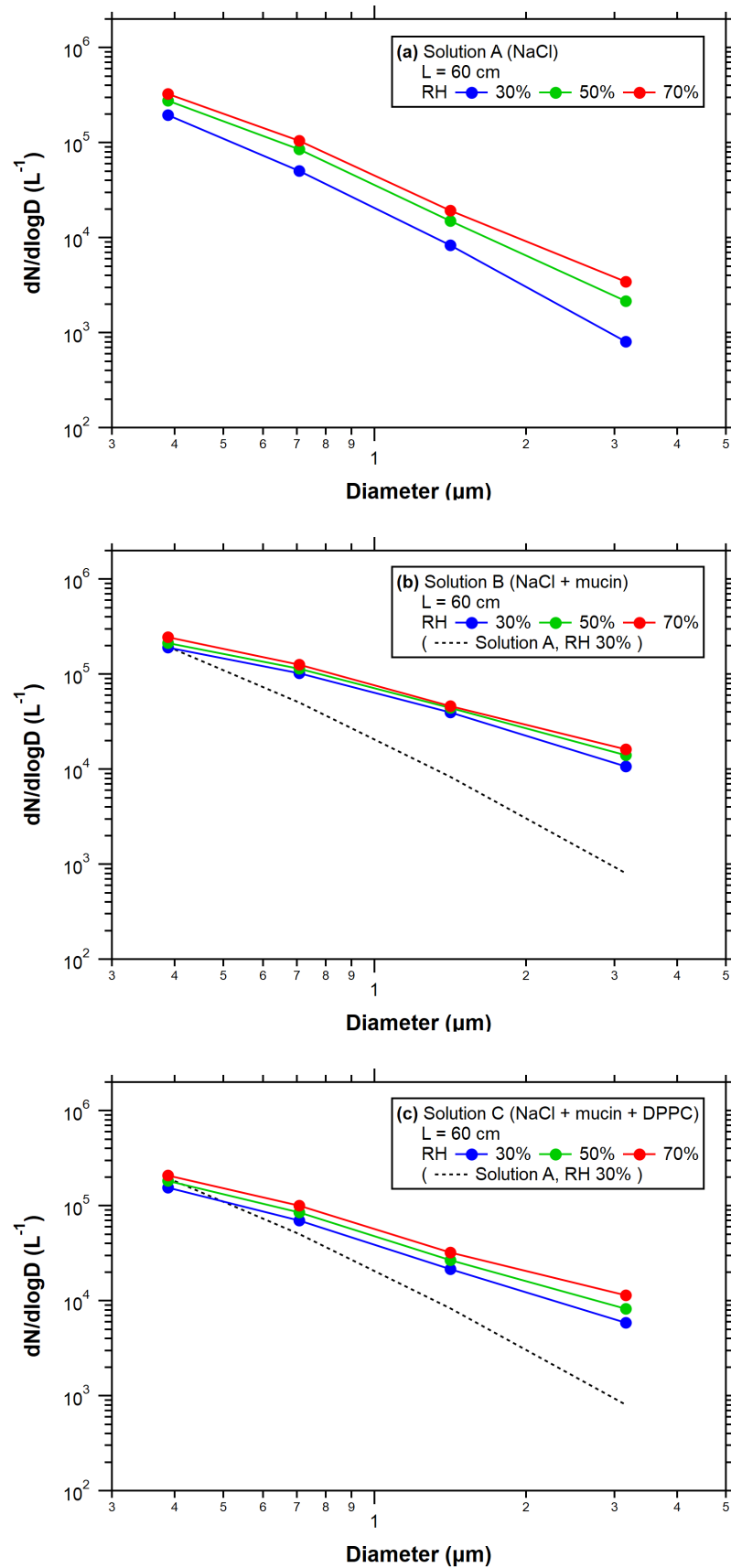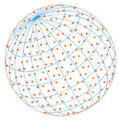
Fig. 5. Approximate particle number size distributions derived by differentiating size-segregated particle number concentrations measured by the OPC for Solutions A, B, and C (*L* = 60 cm).
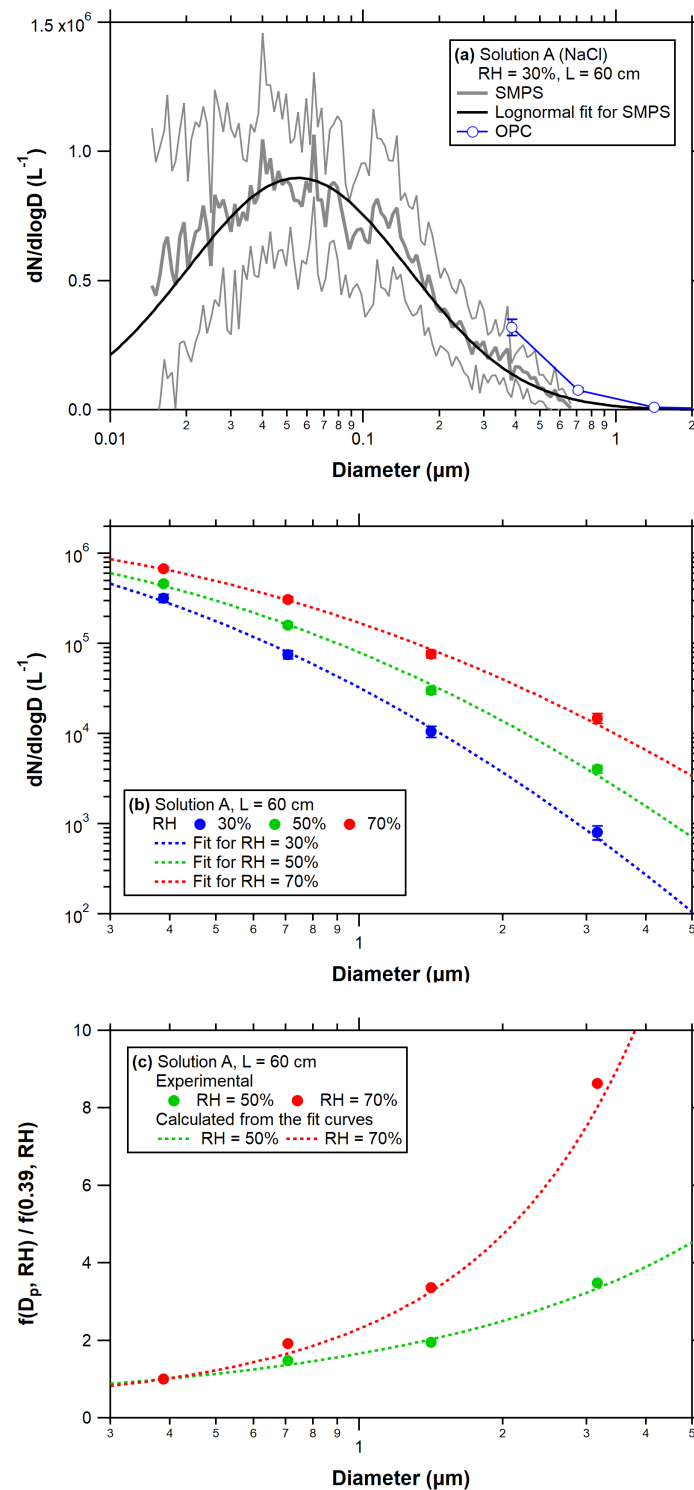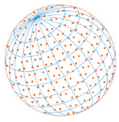
Fig. 6. (a) Particle number size distributions for Solution A (RH = 30%, *L* = 60 cm) obtained by the SMPS (shaded lines) and OPC (open circles). The thick shaded line represents the average of repeated SMPS measurements, and the thin shaded lines represent the range of one standard deviation. The lognormal fitting curve for the SMPS data is shown by the solid line. (b) Particle number size distributions at each RH for Solution A obtained by the OPC (*L* = 60 cm) and the lognormal fitting curves as constrained by the geometric mean diameter derived from the SMPS fitting. (c) $f(D_p, RH)/f(0.39, RH)$ ratios for RH = 50% and 70% as a function of D_p derived from the results in (b). The solid circles represent the ratios derived from the experimental data. The dashed lines represent the ratios calculated from the fitting curves.
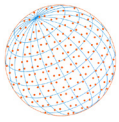
Fig. 6(c) shows the $f(D_p, RH)/f(0.39, RH)$ ratios for RH = 50% and 70% as a function of D_p derived from the experimental data and calculated from the fitting curves in Fig. 6(b), where D_p = 0.39 μm corresponds to the center diameter of the lowest size bin of the differentiated OPC data. The $r(RH, s)$ term has been cancelled out by calculating the ratios. The increase in the $f(D_p, RH)/f(0.39, RH)$ ratios with increasing D_p and RH reflects the shift in the particle number size distributions due to the hygroscopic growth of the NaCl particles. Similarly to NaCl, highly hygroscopic particles (strong RH dependency) are expected to show systematic increases in the $f(D_p, RH)/f(0.39, RH)$ ratios with increasing D_p and RH. Conversely, less hygroscopic particles (weak RH dependency) are expected to show only slight increases in the $f(D_p, RH)/f(0.39, RH)$ ratios with increasing D_p and RH. Therefore, changes in the $f(D_p, RH)/f(0.39, RH)$ ratios as a function of D_p and RH within a RH modulation cycle (RH = 70, 50, 30, and 70%) could be used as a diagnostic for the hygroscopicity of the particles.

3.3 Dependency on Particle Diameter and Relative Humidity

Fig. 7 shows the $f(D_p, RH)/f(0.39, RH)$ ratios for RH = 50% and 70% as a function of D_p for Solutions A, B, and C. All of the datasets, each of which corresponds to a RH modulation cycle, are plotted. The $f(D_p, RH)/f(0.39, RH)$ ratios for Solution A showed systematic increases with increasing D_p and RH for each dataset. The $f(D_p, RH)/f(0.39, RH)$ ratios did not show significant dependency on the L values, suggesting that the residence time of 1 s (L = 20 cm) was sufficient for achieving water equilibrium. Therefore, the small difference in the σ values for RH = 30%, 50%, and 70% derived from the data in Fig. 6(b) (see Section 3.2) was unlikely due to non-equilibrium
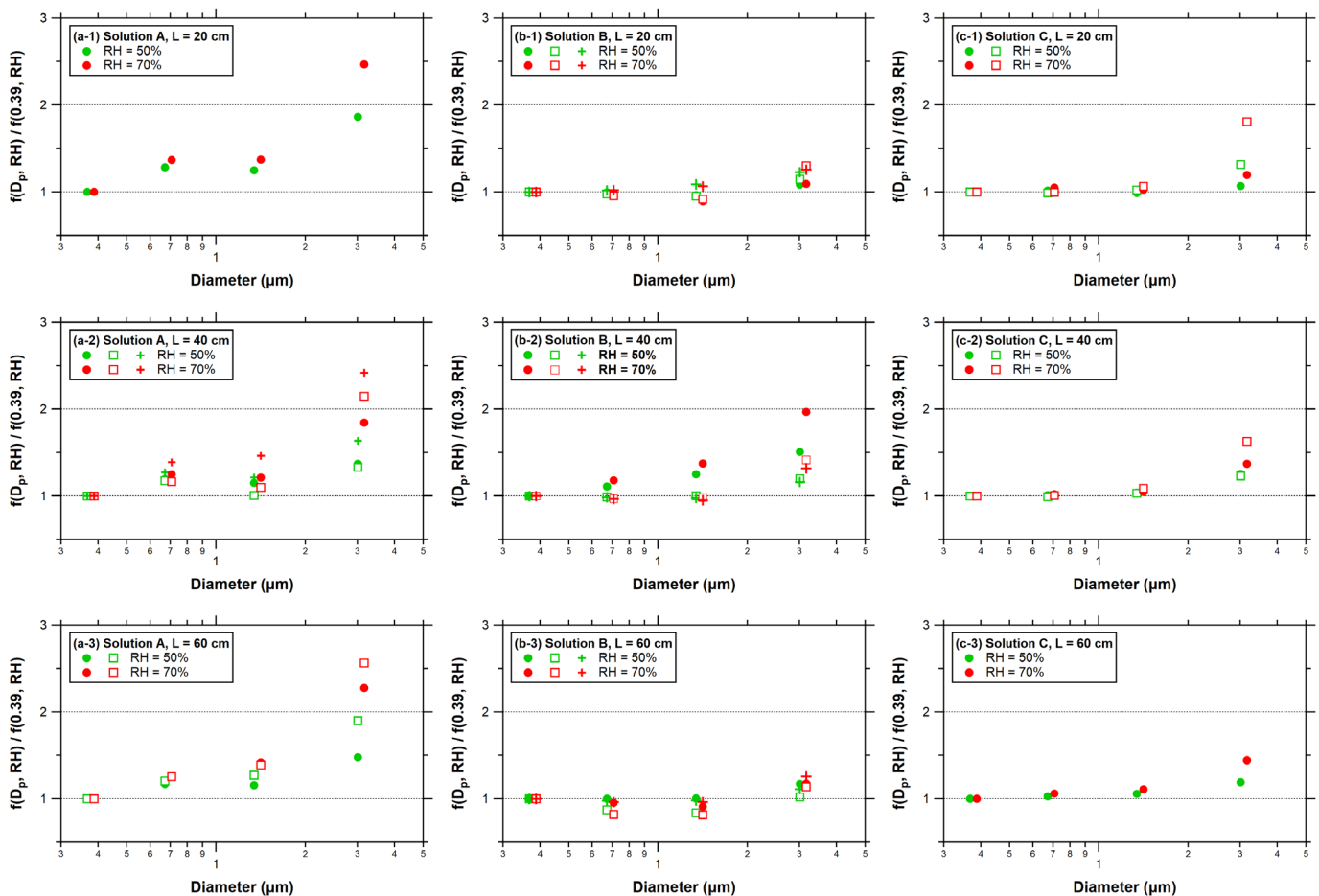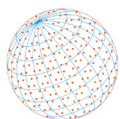

Fig. 7. $f(D_p, RH)/f(0.39, RH)$ ratios for RH = 50% and 70% as a function of D_p for Solutions A, B, and C. The difference in the symbols (solid circles, open squares, and crosses) represents the difference in the datasets, each of which corresponds to a RH modulation cycle (RH = 70%, 50%, 30%, and 70%). The data points for RH = 50% were shifted for clarity.

states of water. We speculate that the difference in the optical diameter between dry (RH = 30%) and wet (RH = 50% and 70%) particles was a possible source of uncertainties in the σ values. It should be noted that the $f(D_p, \text{RH})/f(0.39, \text{RH})$ ratios for Solution A in Fig. 7 were much smaller than those in Fig. 6(c). The absolute values of the $f(D_p, \text{RH})/f(0.39, \text{RH})$ ratios can vary depending on D_m and σ (not available for the datasets shown in Fig. 7), which is another limitation for the interpretation of the data. Nevertheless, the distinct increases in the $f(D_p, \text{RH})/f(0.39, \text{RH})$ ratios qualitatively indicate the high hygroscopicity of NaCl particles.

The $f(D_p, \text{RH})/f(0.39, \text{RH})$ ratios for Solutions B and C showed only small changes with increasing D_p and RH for each dataset and did not show systematic dependency on the L values. These results suggest that the RH dependency of the particle number size distributions was very weak at least over a time scale of a few seconds. Furthermore, some datasets for Solutions B and C showed almost no RH dependency (i.e., the $f(D_p, \text{RH})/f(0.39, \text{RH})$ ratios of ~1 in Fig. 7). The scatter in the data points for Solutions B and C suggests that the reproducibility (or stability) of the results for Solution C was higher than that for Solution B.

4 DISCUSSION

The hygroscopic growth factor for porcine stomach mucin particles has not been previously reported. Groth et al. (2023) investigated the hygroscopicity of porcine respiratory aerosols containing mucin and showed a hygroscopic growth factor of ~1.1 at RH = 70% (relative to RH = 30%). Johnson et al. (1996) investigated the hygroscopicity of DPPC particles and found no significant hygroscopic growth even at RH = 70%. The mixing of NaCl with mucin and DPPC in Solutions B and C may have weakened the RH dependency compared to pure NaCl particles because of the less hygroscopic properties of mucin and DPPC particles. However, the datasets exhibiting almost no RH dependency (the $f(D_p, \text{RH})/f(0.39, \text{RH})$ ratios of ~1 in Fig. 7) may not be explained by the above mechanism.

Huynh et al. (2022) found that a protein-enriched shell with aqueous inorganic core could be formed in a droplet during the evaporation of water. If mucin shells were formed in the droplets generated from Solutions B and C, they might have suppressed further evaporation of water from the droplets after a large fraction of water was evaporated within ~1 s. This mechanism can potentially explain the very weak RH dependency of the particle number size distributions at least over a time scale of a few seconds. The addition of DPPC, which tends to concentrate at the gas-liquid interface, may have interfered with the formation of the mucin shells. Bartkowiak et al. (2019) investigated the interaction of mucin and DPPC at the gas-liquid interface of bulk solutions and found that the formation of a mucin layer beneath a DPPC layer stiffens and stabilizes the structure of the system. Seyfert et al. (2022) observed the morphology of droplet nuclei for NaCl, (NaCl + mucin), and (NaCl + mucin + DPPC) particles and found complex structural changes in the particles containing DPPC. However, it is uncertain how such structural changes of particles affected the hygroscopic measurements for Solution C. Further investigation is needed to quantify the role of mucin and DPPC in affecting the mass transfer of water molecules and the structures of particles during the drying processes.

5 CONCLUSIONS

We investigated the evaporation of water from airborne model respiratory droplets containing NaCl, mucin, and DPPC on the time scale of the order of seconds by conducting flow tube experiments. Size-segregated particle number concentrations were measured at flow tube RH of 30%, 50%, and 70%. The particle number size distributions for NaCl exhibited systematic changes with an increasing RH. The particle number size distributions for (NaCl + mucin) and (NaCl + mucin + DPPC) exhibited very weak RH dependency. These results suggest that the presence of mucin and DPPC had a significant effect on the RH dependency for the evaporation of water from the model droplets.

Considering the microscopic observations of evaporating droplets reported by previous studies, the RH dependency of the particle number size distributions suggests that mucin might have formed shells at the gas-liquid interface of the droplets. The addition of DPPC may have caused
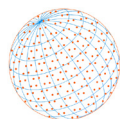
structural changes inside the droplet or at the gas-liquid interface. Further investigation is needed to quantify the role of mucin and DPPC in affecting the mass transfer of water molecules and the structures of particles during the drying processes.

ACKNOWLEDGMENTS

DISCLAIMER

Publication of this article does not imply recommendation or endorsement of any commercial products by the authors.

REFERENCES

Bartkowiak, A., Rojewska, M., Prochaska, K. (2019). Study of mucin interaction with model phospholipid membrane at the air–water interface. Colloids Surf., A 578, 123587. https://doi.org/10.1016/j.colsurfa.2019.123587

Božič, A., Kanduč, M. (2021). Relative humidity in droplet and airborne transmission of disease. J. Biol. Phys. 47, 1–29. https://doi.org/10.1007/s10867-020-09562-5

Chien, C.H., Theodore, A., Wu, C.Y., Hsu, Y.M., Birky, B. (2016). Upon correlating diameters measured by optical particle counters and aerodynamic particle sizers. J. Aerosol Sci. 101, 77–85. https://doi.org/10.1016/j.jaerosci.2016.05.011

Davies, J.F., Price, C.L., Choczynski, J., Kohli, R.K. (2021). Hygroscopic growth of simulated lung fluid aerosol particles under ambient environmental conditions. Chem. Commun. 57, 3243–3246. https://doi.org/10.1039/D1CC00066G

Freedman, M.A. (2020). Liquid-liquid phase separation in supermicrometer and submicrometer aerosol particles. Acc. Chem. Res. 53, 1102–1110. https://doi.org/10.1021/acs.accounts.0c00093

Groth, R., Niazi, S., Spann, K., Johnson, G.R., Ristovski, Z. (2023). Physicochemical characterization of porcine respiratory aerosol and considerations for future aerovirology. PNAS Nexus. 2, 1–10. https://doi.org/10.1093/pnasnexus/pgad087

Hinds, W.C. (1999). Aerosol Technology: Properties, Behavior, and Measurement of Airborne Particles, 2nd ed., John Wiley, Hoboken, N. J.

Huynh, E., Olinger, A., Woolley, D., Kohli, R.K., Choczynski, J.M., Davies, J.F., Lin, K., Marr, L.C., Davis, R.D. (2022). Evidence for a semisolid phase state of aerosols and droplets relevant to the airborne and surface survival of pathogens. Proc. Natl. Acad. Sci. U.S.A. 119, e2109750119. https://doi.org/10.1073/pnas.2109750119

Johnson, D.L., Wenger, E.N., Polikandiitou-Lambros, M. (1996). Aerosolization and hygroscopic growth evaluation of lyophilized liposome aerosols under controlled temperature and relative humidity conditions. Aerosol Sci. Technol. 25, 22–30. https://doi.org/10.1080/02786829608965376

Kormuth, K.A., Lin, K., Prussin, A.J., Vejerano, E.P., Tiwari, A.J., Cox, S.S., Myerburg, M.M., Lakdawala, S.S., Marr, L.C. (2018). Influenza virus infectivity is retained in aerosols and droplets independent of relative humidity. J. Infect. Dis. 218, 739–747. https://doi.org/10.1093/infdis/jiy221

Leung, N.H.L. (2021). Transmissibility and transmission of respiratory viruses. Nat. Rev. Microbiol. 19, 528–545. https://doi.org/10.1038/s41579-021-00535-6

Lieber, C., Melekidis, S., Koch, R., Bauer, H.J. (2021). Insights into the evaporation characteristics of saliva droplets and aerosols: Levitation experiments and numerical modeling. J. Aerosol Sci. 154, 105760. https://doi.org/10.1016/j.jaerosci.2021.105760

Lin, K., Schulte, C.R., Marr, L.C. (2020). Survival of MS2 and Φ6 viruses in droplets as a function of relative humidity, pH, and salt, protein, and surfactant concentrations. PLoS One 15, e0243505. https://doi.org/10.1371/journal.pone.0243505
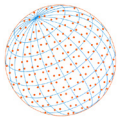
Liu, P., Song, M., Zhao, T., Gunthe, S.S., Ham, S., He, Y., Qin, Y.M., Gong, Z., Amorim, J., Bertram, A.K., Martin, S. (2018). Resolving the mechanisms of hygroscopic growth and cloud condensation nuclei activity for organic particulate matter. Nat. Commun. 9, 4076. https://doi.org/10.1038/s41467-018-06622-2

Meister, T.L., Dreismeier, M., Blanco, E.V., Bruggemann, Y., Heinen, N., Kampf, G., Todt, D., Nguyen, H.P., Steinmann, J., Schmidt, W.E., Steinmann, E., Quast, D.R., Pfaender, S. (2022). Low risk of severe acute respiratory syndrome coronavirus 2 transmission by fomites: A clinical observational study in highly infectious coronavirus disease 2019 patients. J. Infect. Dis. 226, 1608–1615. https://doi.org/10.1093/infdis/jiac170

Morris, D.H., Yinda, K.C., Gamble, A., Rossine, F.W., Huang, Q., Bushmaker, T., Fischer, R.J., Matson, M.J., Van Doremalen, N., Vikesland, P.J., Marr, L.C., Munster, V.J., Lloyd-Smith, J.O. (2021). Mechanistic theory predicts the effects of temperature and humidity on inactivation of SARS-CoV-2 and other enveloped viruses. eLife 10, e65902. https://doi.org/10.7554/eLife.65902

Mikhailov, E., Vlasenko, S., Niessner, R., Pöschl, U. (2004). Interaction of aerosol particles composed of protein and salts with water vapor: hygroscopic growth and microstructural rearrangement, Atmos. Chem. Phys. 4, 323–350. https://doi.org/10.5194/acp-4-323-2004

Mikhailov, E.F., Pöhlker, M.L., Reinmuth-Selzle, K., Vlasenko, S.S., Krüger, O.O., Fröhlich-Nowoisky, J., Pöhlker, C., Ivanova, O.A., Kiselev, A.A., Kremper, L.A., Pöschl, U. (2021). Water uptake of subpollen aerosol particles: hygroscopic growth, cloud condensation nuclei activation, and liquid-liquid phase separation. Atmos. Chem. Phys. 21, 6999–7022. https://doi.org/10.5194/acp-21-6999-2021

Morawska, L., Milton, D.K. (2020). It is time to address airborne transmission of coronavirus disease 2019 (COVID-19). Clin. Infect. Dis. 71, 2311–2313. https://doi.org/10.1093/cid/ciaa939

Piana, A., Colucci, M.E., Valeriani, F., Marcolongo, A., Sotgiu, G., Pasquarella, C., Margarucci, L.M., Petrucca, A., Gianfranceschi, G., Babudieri, S., Vitali, P., D'Ermo, G., Bizzarro, A., De Maio, F., Vitali, M., Azara, A., Romano, F., Simmaco, M., Romano Spica, V. (2021). Monitoring COVID-19 transmission risks by quantitative real-time PCR tracing of droplets in hospital and living environments. mSphere 6, e01070-20. https://doi.org/10.1128/mSphere.01070-20

Prussin, A.J., Schwake, D.O., Lin, K., Gallagher, D.L., Buttling, L., Marr, L.C. (2018). Survival of the enveloped virus phi 6 in droplets as a function of relative humidity, absolute humidity, and temperature. Appl. Environ. Microbiol. 84, e00551-18. https://doi.org/10.1128/AEM.00551-18

Rezaei, M., Netz, R.R. (2021). Airborne virus transmission via respiratory droplets: Effects of droplet evaporation and sedimentation. Curr. Opin. Colloid Interface Sci. 55, 101471. https://doi.org/10.1016/j.cocis.2021.101471

Robey, A.J., Fierce, L. (2022). Sensitivity of airborne transmission of enveloped viruses to seasonal variation in indoor relative humidity. Int. J. Heat Mass Transf. 130, 105747. https://doi.org/10.1016/j.icheatmasstransfer.2021.105747

Seyfert, C., Rodríguez-Rodríguez, J., Lohse, D., Marin, A. (2022). Stability of respiratory-like droplets under evaporation. Phys. Rev. Lett. 7, 023603. https://doi.org/10.1103/PhysRevFluids.7.023603

Vejerano, E.P., Marr, L.C. (2018). Physico-chemical characteristics of evaporating respiratory fluid droplets. J. R. Soc. Interface 15, 20170939. https://doi.org/10.1098/rsif.2017.0939

Walker, J.S., Archer, J., Gregson, F.K.A., Michel, S.E.S., Bzdek, B.R., Reid, J.P. (2021). Accurate representations of the microphysical processes occurring during the transport of exhaled aerosols and droplets. ACS Cent. Sci. 7, 200–209. https://doi.org/10.1021/acscentsci.0c01522

Wang, C.C., Prather, K.A., Sznitman, J., Jimenez, J.L., Lakdawala, S.S., Tufekci, Z., Marr, L.C. (2021). Airborne transmission of respiratory viruses. Science 373, 6558. https://doi.org/10.1126/science.abd9149

World Health Organization (WHO) (2020). Modes of transmission of virus causing COVID-19: Implications for IPC precaution recommendations: scientific brief. 27 March 2020. https://www.who.int/news-room/commentaries/detail/modes-of-transmission-of-virus-causing-covid-19-implications-for-ipc-precaution-recommendations (accessed 03 January 2021).

Yang, W., Marr, L.C. (2011). Dynamics of airborne influenza A viruses indoors and dependence on humidity. PLoS One 6, e21481. https://doi.org/10.1371/journal.pone.0021481

Yang, W., Marr, L.C. (2012). Mechanisms by which ambient humidity may affect viruses in aerosols. Appl. Environ. Microbiol. 78, 6781–6788. https://doi.org/10.1128/AEM.01658-12
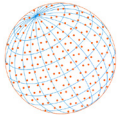
Zhou, L., Ayeh, S.K., Chidambaram, V., Karakousis, P.C. (2021). Modes of transmission of SARS-CoV-2 and evidence for preventive behavioral interventions. BMC Infect. Dis. 21, 496. https://doi.org/10.1186/s12879-021-06222-4

Zieger, P., Väisänen, O., Corbin, J.C., Partridge, D.G., Bastelberger, S., Mousavi-Fard, M., Rosati, B., Gysel, M., Krieger, U.K., Leck, C., Nenes, A., Riipinen, I., Virtanen, A., Salter, M.E. (2017). Revising the hygroscopicity of inorganic sea salt particles. Nat. Commun. 8, 15883. https://doi.org/10.1038/ncomms15883